



Contents lists available at ScienceDirect

International Communications in Heat and Mass Transfer

journal homepage: www.elsevier.com/locate/ichmt

The effect of viscous heating on the linear and nonlinear stability analysis of a flow through a porous duct

Michele Celli^{a,*}, Antonio Barletta^a, Pedro Vayssiére Brandão^a, Silvia da Costa Hirata^b, Mohamed Najib Ouarzazi^b

^a Department of Industrial Engineering, Alma Mater Studiorum Università di Bologna, Viale Risorgimento 2, Bologna 40136, Italy

^b Unité de Mécanique de Lille, Université de Lille, Bd. Paul Langevin 1, Villeneuve d'Ascq, Cedex 59655, France

ARTICLE INFO

Keywords:

Thermal convection
Porous medium
Dual solution
Linear stability analysis
Nonlinear stability analysis

ABSTRACT

The stability of a stationary fully developed vertical flow across a porous pipe is investigated. The heating due to viscous dissipation is assumed to be non-negligible and also to be the only effect triggering the onset of thermal convection. An innovative scaling is employed to study the case of small Gebhart number. The viscous heating term present inside the energy balance equation yields a basic stationary flow characterised by dual branches of solutions: for a given vertical pressure gradient, two possible velocity profiles are obtained. The linear and nonlinear stability of the stationary dual solutions is performed. The linear stability is investigated in a usual fashion by employing the normal modes method and then solving the eigenvalue problem obtained by using the shooting method. The nonlinear stability is investigated by simulating numerically the evolution in time of the perturbed system. The linear stability analysis allows one to conclude that the critical wavenumber for the onset of instability is zero and the critical dimensionless velocity at the pipe axis is equal to 3.43631. The results of the nonlinear analysis display subcritical instabilities. Indeed, the onset of instability is obtained for values of the governing parameters which are lower than the critical values obtained by the linear analysis. This feature occurs when the amplitude of the initial disturbance applied to the nonlinear problem is sufficiently high, namely when the dimensionless amplitude is larger than 10^{-2} .

1. Introduction

The effect of viscous dissipation on the heat and mass transfer in vertical channels is a topic widely studied in the recent literature. In the last decade, a great attention has been devoted to the effect of viscous dissipation and to the nonlinearity in the onset of thermal convection [1–4]. In particular, for vertical channels, the free and mixed convection has been investigated by Barletta [5,6]. When the viscous dissipation term is present inside the energy balance equation, the solutions of the basic stationary state may become dual: for a given basic pressure gradient or a given mass flow rate, more than one velocity profile has been obtained by Barletta et al. [7,8], Barletta and Celli [9].

The study of the conditions for the onset of thermal convection in a vertical plane channel relies on a necessary condition: the presence of a suitable stationary temperature gradient inside the domain as investigated by Gill and Davey [10], Vest and Arpacı [11], Korpela et al. [12],

McBain and Armfield [13]. This temperature gradient may trigger the onset of thermal instability. A number of effects may produce and maintain this temperature gradient and, most frequently, it is forced by suitable boundary conditions. When the boundary conditions do not produce a temperature gradient, this can be generated by the internal heating due to viscous dissipation Deepika et al. [2], Straughan [14], Rees and Magyari [15], Barletta and Mulone [16]. The stability of dual stationary solutions which may arise when viscous dissipation is considered has been investigated by Miklavčič and Wang [17], Miklavčič [18].

Besides the investigation of convective fluid flows in vertical channels, an interesting topic is the study of thermal convection in vertical fluid saturated porous channels. Several papers investigating the stability of a fluid saturated porous medium with respect to thermal convection are present in the literature. For an exhaustive review we refer to the book by Nield and Bejan [19]. When vertical fluid saturated porous

* Corresponding author.

E-mail addresses: michele.cellis3@unibo.it (M. Celli), antonio.barletta@unibo.it (A. Barletta), pedro.vayssiere2@unibo.it (P.V. Brandão), silvia.hirata@univ-lille.fr (S. da Costa Hirata), mohamed-najib.ouarzazi@univ-lille.fr (M.N. Ouarzazi).

<https://doi.org/10.1016/j.icheatmasstransfer.2024.107712>

channels are analysed by taking into account the viscous heating effect, the literature presents a less abundant number of studies. One may refer to Barletta et al. [20], Barletta and Miklavčič [21].

The present paper studies the role of viscous dissipation for the onset of thermal convection in an impermeable vertical pipe bounded by an isothermal wall and subject to a prescribed vertical pressure gradient. Both the linear and nonlinear stability analysis of the dual basic stationary solutions are carried out numerically in the limit of small Gebhart number.

The topic investigated is significant for a number of applications related both to geophysical research and to engineering design. Possible applications include the analysis of water currents in porous reservoirs, underground spreading of pollutants, CO₂ sequestration, oil extraction engineering, enhancement of the performance in building insulation.

2. Mathematical model

A fluid saturated vertical porous duct subject to a given vertical pressure gradient is investigated. The geometrical configuration of the system studied is presented in Fig. 1. The cylindrical duct has a circular cross-section of radius r_0 and it is characterised by a uniform temperature at the boundary. The duct boundary is impermeable. The imposed vertical pressure gradient, either positive or negative, produces a net mass flow rate. Darcy's law together with the Oberbeck-Boussinesq approximation is employed to model the buoyant flow. The fluid is assumed to be Newtonian. The local energy balance employed is the conduction/convection equation where a heat generation due to viscous dissipation is considered [19]. Thus, the flow regime is one of mixed convection. The governing equations are the following:

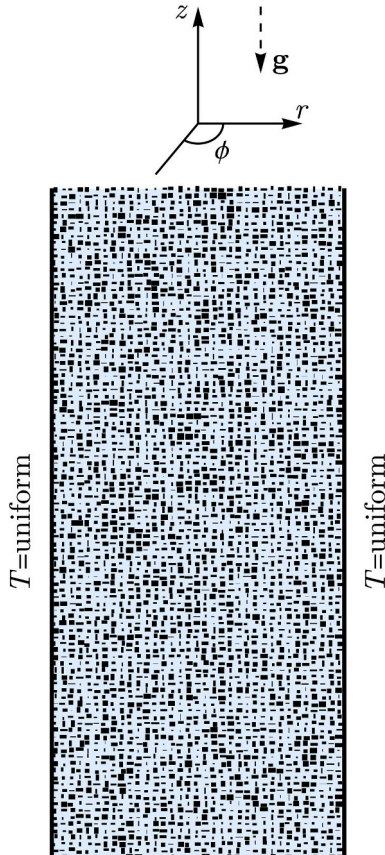


Fig. 1. Qualitative drawing of the geometry and the boundary condition.

$$\nabla \cdot \mathbf{u} = 0,$$

$$\frac{\mu}{K} \mathbf{u} = -\nabla p - \rho \beta (T - T_0) \mathbf{g}$$

$$\sigma \frac{\partial T}{\partial t} + \mathbf{u} \cdot \nabla T = \alpha \nabla^2 T + \mu \Phi, \tag{1}$$

$$r = r_0 : \begin{cases} u = 0, \\ \frac{\partial T}{\partial z} = 0, \quad \frac{\partial T}{\partial \phi} = 0, \end{cases}$$

where the dissipation function is given by

$$\Phi = \frac{\mathbf{u} \cdot \mathbf{u}}{\rho c K}, \tag{2}$$

and the cylindrical coordinates (r, ϕ, z) are employed. Moreover, $\mathbf{u} = (u, v, w)$ is the velocity vector in the (r, ϕ, z) directions, μ is the dynamic viscosity of the fluid, K is the permeability of the porous medium, p is the local difference between the pressure and the hydrostatic pressure, ρ is the density of the fluid evaluated at the reference temperature T_0 , \mathbf{g} is the modulus of the gravity acceleration vector \mathbf{g} , β is the thermal expansion coefficient of the fluid evaluated at T_0 , T is the temperature of the fluid saturated porous medium, \mathbf{e}_z is the unit vector along the z -direction, σ is the ratio between the average volumetric heat capacity of the porous medium and the volumetric heat capacity of the fluid, α is thermal diffusivity of the fluid saturated porous medium, and c is the specific heat of the fluid. The reference temperature T_0 is chosen as the average temperature on the duct cross-section S , namely

$$T_0 = \frac{1}{S} \iint_S T dS. \tag{3}$$

The dimensionless (primed) quantities are defined as

$$(r, z) = r_0 (r', z'), \quad t = \frac{\sigma r_0^2}{\alpha} t', \quad (u, v, w) = \frac{\alpha}{Ge r_0} (u', v', w'), \tag{4}$$

$$T = T_0 + \Delta T T', \quad p = \frac{\mu \alpha}{Ge K} p',$$

and are employed to obtain a dimensionless formulation of the governing equations. The Gebhart number Ge and the reference temperature difference ΔT are defined as follows:

$$Ge = \frac{g \beta r_0}{c}, \quad \Delta T = \frac{\mu \alpha}{Ge^2 K \rho c}. \tag{5}$$

Hereafter, for the sake of brevity, we will omit the primes for the dimensionless quantities. By applying the scaling (4) to Eq. (1), we obtain

$$\nabla \cdot \mathbf{u} = 0,$$

$$\mathbf{u} = -\nabla p + T \mathbf{e}_z,$$

$$\frac{\partial T}{\partial t} + \frac{1}{Ge} \mathbf{u} \cdot \nabla T = \nabla^2 T + \mathbf{u} \cdot \mathbf{u}, \tag{6}$$

$$r = 1 : \begin{cases} u = 0, \\ \frac{\partial T}{\partial z} = 0, \quad \frac{\partial T}{\partial \phi} = 0. \end{cases}$$

The reference temperature defined in Eq. (3) yields the dimensionless constraint

$$\int_0^1 \int_0^{2\pi} T r dr d\phi = 0. \tag{7}$$

The Gebhart number is a dimensionless parameter that drives the intensity of the viscous dissipation effect. This effect is, for the everyday life applications, typically much lower than unity. There are cases where the value of the Gebhart number can be of order unity but such cases are

almost exclusively of geophysical or astrophysical interest.

3. Stationary dual solutions

Among all the possible solutions of the system (6), we consider the fully developed flows characterised by the sole axial component. For simplicity, we disregard the angular dependence, so that the axial velocity depends only on the radial coordinate. The circular symmetry in the temperature boundary conditions implies that also the temperature field depends only on the radial coordinate. Darcy’s law, for the basic state just described, yields a pressure p that is independent of r and ϕ with $d^2p_b/dz^2 = 0$. By considering the assumptions just presented, Eq. (6) simplifies to

$$\begin{aligned} w_b &= T_b + 2\Pi, \\ \frac{d^2w_b}{dr^2} + \frac{1}{r} \frac{dw_b}{dr} + w_b^2 &= 0, \\ r = 0 : \quad \frac{dw_b}{dr} &= 0, \end{aligned} \tag{8}$$

where the subscript b denotes the basic state and

$$\Pi = -\frac{1}{2} \frac{dp_b}{dz} \tag{9}$$

The first Eq. (8) is the vertical component of the second Eq. (6), while the second Eq. (8) is the third Eq. (6) where T_b is expressed in terms of w_b . The condition $dw_b/dr = 0$ imposed at the duct axis can be applied because the basic velocity is assumed to be axisymmetric and with a finite second-order derivative at $r = 0$. The constraint in Eq. (7) allows one to obtain the basic flow rate for the velocity profile,

$$\int_0^1 w_b r dr = \Pi. \tag{10}$$

The system Eq. (8) is solved as an initial value problem, namely

$$\begin{aligned} \frac{d^2w_b}{dr^2} + \frac{1}{r} \frac{dw_b}{dr} + w_b^2 &= 0, \\ r = \epsilon : \quad w_b = \eta, \quad \frac{dw_b}{dr} &= 0, \end{aligned} \tag{11}$$

where $\eta = w_b(0)$ is the unknown velocity at pipe axis and ϵ is a cut-off parameter employed to encompass the numerical issues due to the singularity at $r = 0$. A discussion of the suitable values of ϵ to be employed is reported in Appendix A: the results obtained throughout the paper are obtained by employing $\epsilon = 10^{-10}$.

The left-hand frame of Fig. 2 displays the solutions of Eq. (11) for different values of η . For each value of η , Eq. (10) yields a single value of Π : the velocity profiles are presented as functions of the radius r . One may note that the velocity is a monotonic decreasing function of r . Moreover, for sufficiently high values of η , a flow reversal is present close to the wall.

The right-hand frame of Fig. 2 evidences that, for every imposed basic pressure gradient Π , two values of the velocity at pipe axis η are possible: two possible velocity profiles are obtained for a given pressure gradient and, hence, two branches of solutions are present. The two branches are bounded by the maximum value of Π where the two branches coincides, namely

$$\Pi_{max} = 1.59421, \quad \eta(\Pi_{max}) = 8.53412. \tag{12}$$

For $\Pi > \Pi_{max}$ no stationary solution is present. In Fig. 2, the red line in the left-hand frame and the red dot in the right-hand frame are relative to the trivial solution $w_b = 0$. The linear and nonlinear stability of the solutions presented in Fig. 2 is investigated in the following sections.

4. Stability analysis for small values of the Gebhart number

The stability of the two basic solution branches are tested by perturbing the velocity, pressure and temperature fields, thus by redefining these fields as a basic state plus a perturbation:

$$\mathbf{u} = \mathbf{u}_b + \mathbf{U}, \quad p = p_b + P, \quad T = T_b + \Theta. \tag{13}$$

By employing Eq. (13) and the scaling

$$zGe \rightarrow z, \quad \frac{1}{Ge^2} P \rightarrow P, \tag{14}$$

which is useful for the limiting case $Ge \rightarrow 0$, to be studied in the next sections, one obtains the following set of governing equations for the disturbances:

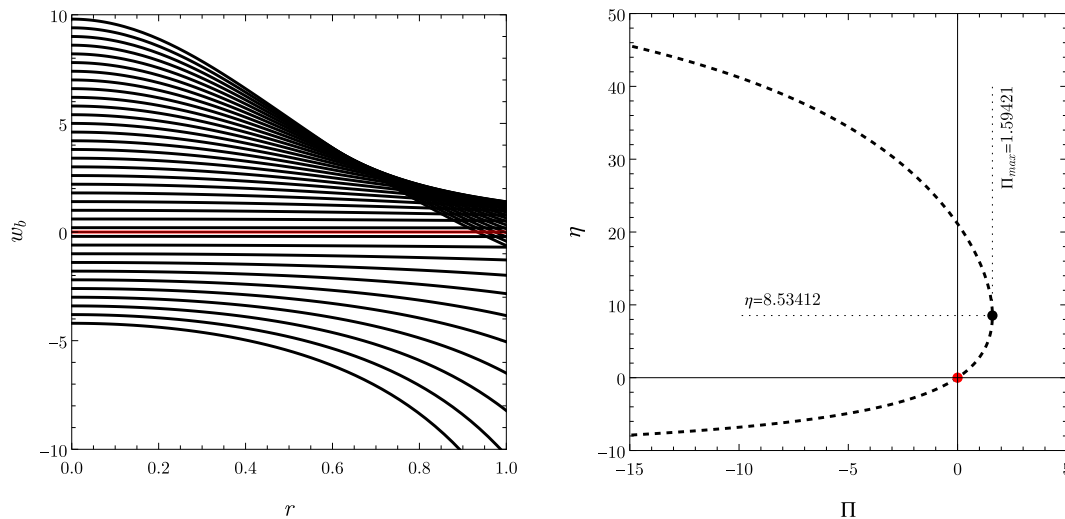


Fig. 2. Left-hand frame: basic state velocity profiles plotted for different values of the duct axis velocity $\eta = w_b(0)$; the red line refers to the $\eta = 0$ and $\Pi = 0$ case. Right-hand frame: representation of the duality of the basic solutions; for a given basic pressure gradient Π we obtain two possible velocities η at the duct axis. The red dot refers to the $\eta = 0$ and $\Pi = 0$ case. (For interpretation of the references to color in this figure legend, the reader is referred to the web version of this article.)

$$\begin{aligned} \frac{\partial U}{\partial r} + \frac{1}{r} \left(U + \frac{\partial V}{\partial \phi} \right) + Ge \frac{\partial W}{\partial z} &= 0, \\ U = -Ge^2 \frac{\partial P}{\partial r}, \quad V = -\frac{Ge^2}{r} \frac{\partial P}{\partial \phi}, \quad W = -Ge^3 \frac{\partial P}{\partial z} + \Theta, \\ \frac{\partial \Theta}{\partial t} + \frac{1}{Ge} \left[U \left(\frac{\partial T_b}{\partial r} + \frac{\partial \Theta}{\partial r} \right) + \frac{V}{r} \frac{\partial \Theta}{\partial \phi} + Ge(w_b + W) \frac{\partial \Theta}{\partial z} \right] &= \\ \frac{\partial^2 \Theta}{\partial r^2} + \frac{1}{r} \frac{\partial \Theta}{\partial r} + \frac{1}{r^2} \frac{\partial^2 \Theta}{\partial \phi^2} + Ge^2 \frac{\partial^2 \Theta}{\partial z^2} + U^2 + V^2 + W^2 + 2w_b W, \\ r = 1 : \quad \frac{\partial \Theta}{\partial z} = \frac{\partial \Theta}{\partial \phi} &= 0. \end{aligned} \tag{15}$$

By recalling that Ge is typically much lower than the unity, the scaling (14) on z produces a zoom-out in the vertical direction. Moreover, by taking the limit $Ge \rightarrow 0$, Eq. (15) yields $U = V = 0$, so that the local mass balance is identically satisfied, and $W = \Theta$. Then we can rewrite Eq. (15) to obtain

$$\begin{aligned} \frac{\partial W}{\partial t} + (w_b + W) \frac{\partial W}{\partial z} &= \\ \frac{\partial^2 W}{\partial r^2} + \frac{1}{r} \frac{\partial W}{\partial r} + \frac{1}{r^2} \frac{\partial^2 W}{\partial \phi^2} + W^2 + 2w_b W, \\ r = 1 : \quad \frac{\partial W}{\partial z} = \frac{\partial W}{\partial \phi} &= 0. \end{aligned} \tag{16}$$

4.1. Linear stability analysis

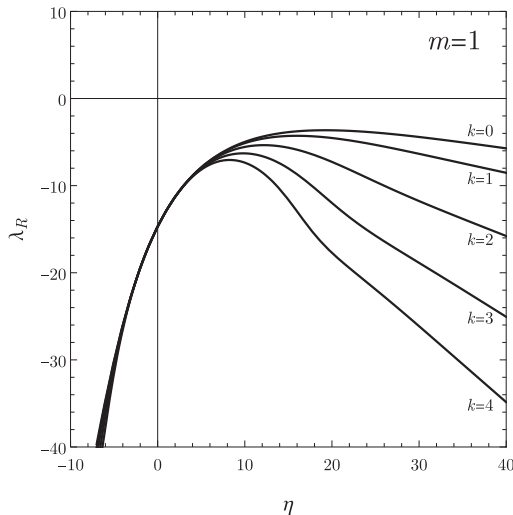
The linear stability of the dual basic solutions reported in Fig. 2 is investigated by linearising Eq. (16) to obtain

$$\begin{aligned} \frac{\partial W}{\partial t} + w_b \frac{\partial W}{\partial z} = \frac{\partial^2 W}{\partial r^2} + \frac{1}{r} \frac{\partial W}{\partial r} + \frac{1}{r^2} \frac{\partial^2 W}{\partial \phi^2} + 2w_b W, \\ r = 1 : \quad \frac{\partial W}{\partial z} = \frac{\partial W}{\partial \phi} = 0. \end{aligned} \tag{17}$$

The stability analysis based on Eq. (17) is carried out by assuming the solutions of Eq. (17) to have the form of normal modes,

$$W(r, \phi, z, t) = \sum_{m=0}^{\infty} c_m h_m(r) \cos(m\phi) e^{\lambda t} e^{ikz}, \tag{18}$$

where h_m is, in general, a complex function, m is a non negative integer, $\lambda = \lambda_R - i\lambda_I$, λ_R is the growth rate of the normal mode, λ_I is its angular frequency, and k is the mode wavenumber. By substituting Eq. (18) into Eq. (17), one obtains



$$\begin{aligned} \frac{d^2 h_m}{dr^2} + \frac{1}{r} \frac{dh_m}{dr} + \left(2w_b - \lambda - \frac{m^2}{r^2} - ikw_b \right) h_m &= 0, \\ r = 1 : \quad h_m &= 0. \end{aligned} \tag{19}$$

The system (19) is solved by employing the shooting method. The second order ordinary differential equation in (19) is solved as an initial value problem by employing a scale fixing condition together with the symmetry condition, namely

$$\begin{aligned} \frac{d^2 h_m}{dr^2} + \frac{1}{r} \frac{dh_m}{dr} + \left(2w_b - \lambda - \frac{m^2}{r^2} - ikw_b \right) h_m &= 0, \\ r = \epsilon : \quad h_m = 1, \quad \frac{dh_m}{dr} &= 0. \end{aligned} \tag{20}$$

For zero growth rates, $\lambda_R = 0$, by shooting the boundary condition in $r = 1$ one obtains the values of the angular frequency λ_I and of η .

The solutions of Eq. (20) are reported in Figs. 3 and 4. We emphasise that, as reported in Fig. 3, the non-axisymmetric modes do not display any positive growth rate. In fact, Fig. 3 suggests that, as no positive growth rate is detected for $m = 1$ and $m = 2$, the only destabilising modes are those with $m = 0$.

The neutral stability condition relative to the axisymmetric modes, $m = 0$, is displayed in Fig. 4. The left-hand and the right-hand frames report the same data, they are just displayed as functions of η (left) or of Π (right). The blue areas denote linearly stable basic states while the green areas denote linearly unstable basic states. The purple areas are relative to those configurations that, due to the duality of the basic solution, could either be stable or unstable. By looking at both frames, one may notice that, for $k > 9.52178$, no instability is present. The right-hand frame of Fig. 4 has a white upper area denoting that no basic stationary state solutions can be obtained for $\Pi > \Pi_{max} = 1.59421$.

Fig. 5 is a manipulation of Fig. 2 where we highlight with green those basic states that, given the results reported in Fig. 4, can manifest the onset of instability. The basic states colored in blue are linearly stable. The mode with $(k, \eta, \Pi) = (0, 3.43631, 1.14419)$ is the unstable mode with the smallest value of η . The unstable basic solutions show positive velocity profiles while, for sufficiently high values of η , they display flow reversal close to the wall.

4.2. Nonlinear stability analysis

The nonlinear stability of the dual basic solutions is investigated by solving the system of Eq. (16) as an initial value problem: we study the evolution in time of the initial perturbation defined for $t = 0$. We solve

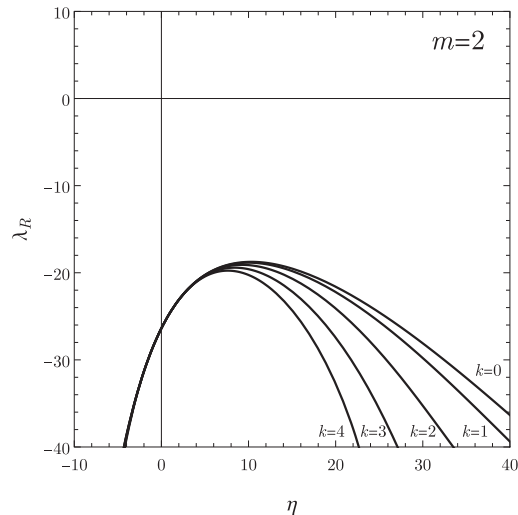


Fig. 3. Growth rates of the disturbances versus η for different values of k : the left-hand frame is drawn for $m = 1$ and right-hand frame for $m = 2$.

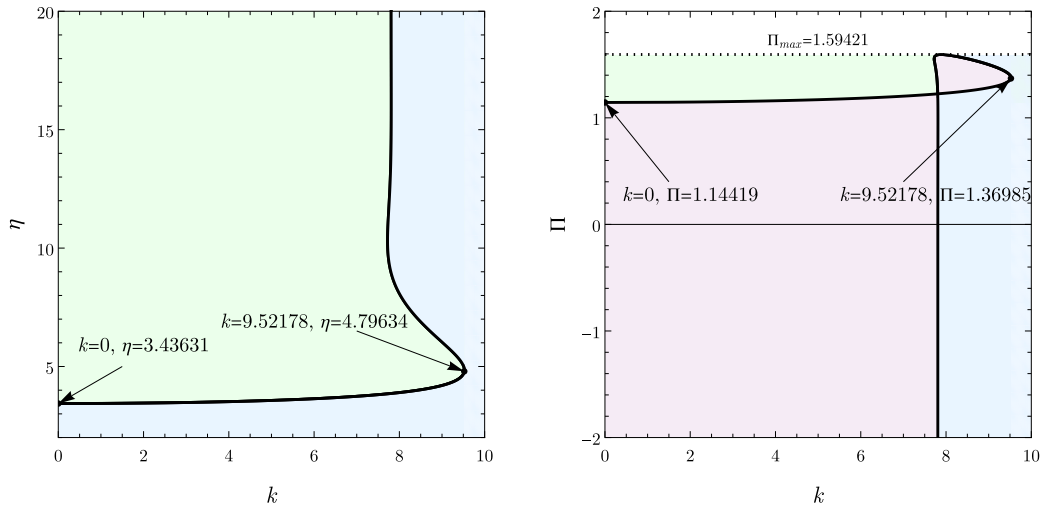


Fig. 4. Linear stability results. Neutral stability curve for $m = 0$ expressed in terms of $\eta(k)$, left-hand frame, and of $\Pi(k)$, right-hand frame. The blue areas are linearly stable while the green areas are linearly unstable. The purple areas define those configurations that, due to the duality of the basic solution, could be either stable or unstable. (For interpretation of the references to color in this figure legend, the reader is referred to the web version of this article.)

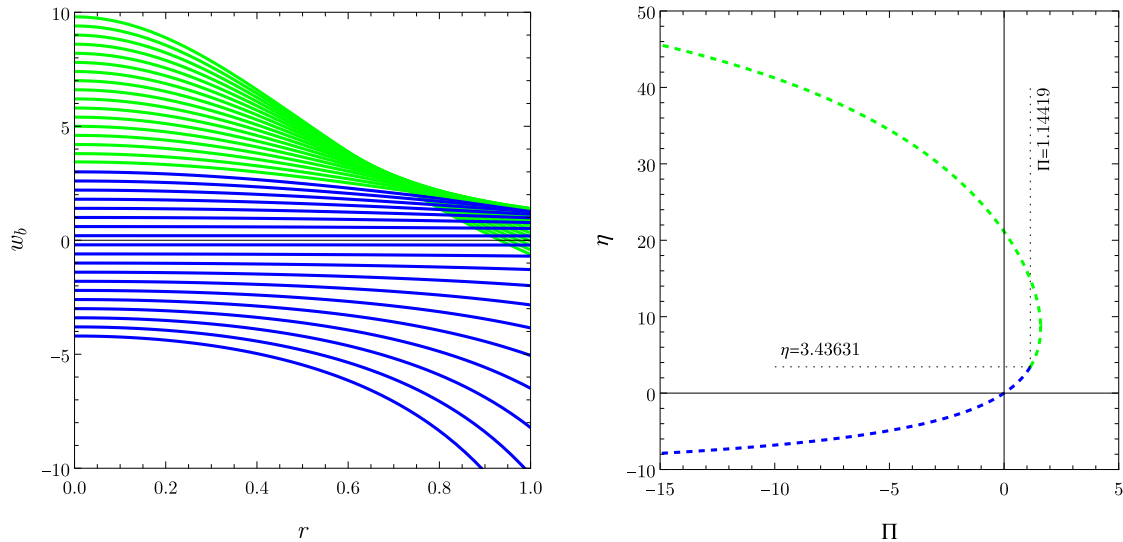


Fig. 5. Linear stability results for the axisymmetric modes, $m = 0$: unstable basic states, green color, and stable basic states, blue color. (For interpretation of the references to color in this figure legend, the reader is referred to the web version of this article.)

numerically the problem

$$\begin{aligned} \frac{\partial W}{\partial t} + (w_b + W) \frac{\partial W}{\partial z} &= \\ \frac{\partial^2 W}{\partial r^2} + \frac{1}{r} \frac{\partial W}{\partial r} + \frac{1}{r^2} \frac{\partial^2 W}{\partial \phi^2} + W^2 + 2w_b W, & \\ t = 0 : \quad W &= A \cos \left[\left(n + \frac{1}{2} \right) \pi r \right], \\ r = 1 : \quad \frac{\partial W}{\partial z} &= \frac{\partial W}{\partial \phi} = 0, \end{aligned} \tag{21}$$

where the initial perturbation is expressed as a radial wave with amplitude A and $n = 0, 1, 2, \dots$. We aim to compare the nonlinear stability results with those obtained by the linear stability analysis. Since in the previous section, for the linear analysis, we concluded that the most unstable case is axisymmetric with an infinite wavelength, $k \rightarrow 0$, we limit our nonlinear investigation to axisymmetric cases independent of z . By employing the Cartesian coordinates, for numerical convenience,

we can rewrite Eq. (21) as

$$\begin{aligned} \frac{\partial W}{\partial t} &= \frac{\partial^2 W}{\partial x^2} + \frac{\partial^2 W}{\partial y^2} + W^2 + 2w_b W, \\ t = 0 : \quad W &= A \cos \left[\left(n + \frac{1}{2} \right) \pi (x^2 + y^2)^{1/2} \right], \\ x^2 + y^2 = 1 : \quad W &= 0, \end{aligned} \tag{22}$$

where the condition $W = 0$ at the wall may be imposed since $W = \Theta$ and the wall is constrained to be at a fixed temperature. Eq. (22) is solved numerically by means of the finite element method implemented by the software environment Mathematica (©Wolfram Research) and its built in function *NDSolve*. A mesh test is reported in Appendix A.

For a given basic state, identified by the value of velocity at the pipe axis η , and for a given value of the initial condition amplitude A and spatial frequency n , we study the evolution in time of the velocity field W . In particular, in Fig. 6 we report, in black, the velocity at the pipe axis $W(r = 0)$ for two different sample cases: the left-hand frame refers to

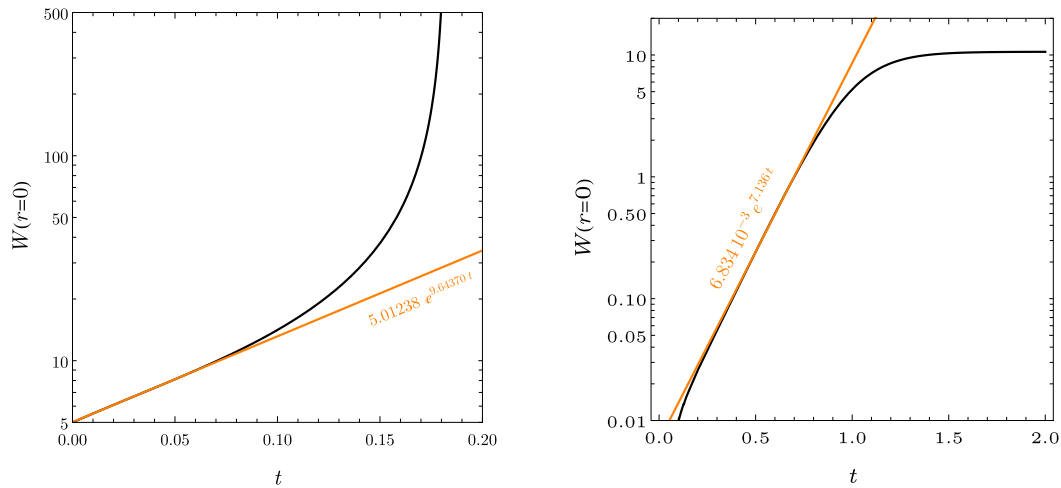


Fig. 6. Nonlinear stability results. Left-hand frame: evolution in time of the velocity at the pipe axis $W(r = 0)$ for $\eta = 5$ and $A = 5$ and $n = 0$. Right-hand frame: evolution in time of the velocity at the pipe axis $W(r = 0)$ for $\eta = 10$, $A = 10^{-2}$, and $n = 1$.

$\eta = 5, A = 5$ and $n = 0$; the right-hand frame refers to $\eta = 10, A = 10^{-2}$ and $n = 1$. We take the velocity at the pipe axis $W(r = 0)$ as a reference velocity to test the stability of the system since, typically, the velocity profile on the pipe cross-section has a maximum located at the pipe axis. The left-hand frame of Fig. 6 represents the typical evolution in time of the unstable initial perturbations characterised by $n = 0$ where, after a sufficiently long time, the velocity at the pipe axis diverges. The right-hand frame represents the typical evolution in time of the unstable initial perturbations characterised by $n = 1$ and $n = 2$ where, after a sufficiently long time, the velocity at the pipe axis tends to a nonlinear equilibrium state, as reported in Fig. 7 for $A = 1$ and $n = 1$. From Fig. 7 one may, by employing a fitting procedure, extrapolate the values of η yielding null values of $W(r = 0)$ at the end of the simulation. These values are reported in Table 1. The values of η reported in Table 1 define a stability threshold that differs from that employed for the linear stability analysis: the linear stability analysis defines the threshold for the onset of instability by looking for null values of the growth rates. For a homogeneous comparison between linear and nonlinear stability results, we thus need to find the growth rates of the unstable nonlinear perturbations. In fact, for both frames of Fig. 6, the orange line represents a nonlinear fit of the exponential growth in time of the

Table 1

Values of η that yield a null velocity at the pipe axis for different values of the amplitude A and for $n = 1$ and $n = 2$.

A	η	
	$n = 1$	$n = 2$
10^{-4}	3.435	3.434
10^{-2}	3.435	3.435
10^{-1}	3.435	3.435
1	3.435	3.435
5	3.435	3.435
10	3.435	3.435

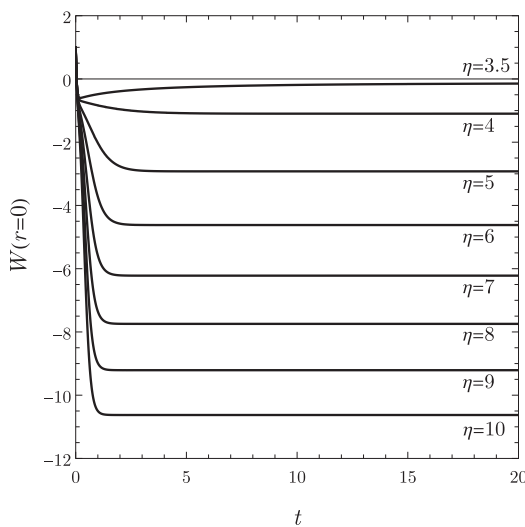


Fig. 7. Nonlinear stability results. Evolution in time of the velocity on the pipe axis $W(r = 0)$ for $A = 1$, $n = 1$ and different values of η .

perturbation. This analysis allows us to draw Fig. 8 where the growth rates are reported, the orange points, as a function of η . The left-hand frame shows the values of λ_R for different values of the initial condition amplitude A and for $n = 0$ while the right-hand frame reports the growth rates for the cases $n = 1$ and $n = 2$. The right-hand frame presents just one curve since the growth rate, for $n > 0$, does not depend in a sensible manner on n and A . By fitting the orange data, we obtained the values of η yielding $\lambda_R = 0$. These data are reported in Table 2 and in Fig. 8 as black dots. In Table 2, for the cases $n = 1$ and $n = 2$, the values obtained for $A > 10^{-1}$ are not present since the growing behaviour is not exponential and the fitting procedure cannot be applied. One may note that, for $n = 0$ and sufficiently low values of the perturbation amplitude A , the linear stability analysis results are recovered with three significant digits while, for sufficiently high values of A , subcritical instabilities are present.

Fig. 9 is an elaboration of Fig. 5 and Fig. 2 where green color denotes those basic states that the linear stability analysis predicts to be unstable; the orange color is for those basic states nonlinearly unstable at subcritical conditions for $n = 0$ and $A = 10$. The basic states displayed in blue are the stable modes. Compared with the linear stability analysis, one may note that also the velocity profiles characterised by purely negative velocities can experience the onset of thermal convection. The mode with $(\eta, \Pi) = (-1.018, -0.5798)$ is the unstable mode with the smallest value of η obtained with the nonlinear stability analysis by imposing $n = 0$ and $A = 10$. We choose this as threshold configuration since the initial conditions characterised by $n = 0$ are those displaying subcritical instabilities. Furthermore, $A = 10$ is a sufficiently high initial perturbation amplitude.

In Fig. 10, we reported the pairs (A, η) relative to the nonlinear threshold values for $n = 0$, black points, together with the critical condition obtained by the linear stability analysis, dotted line. One may

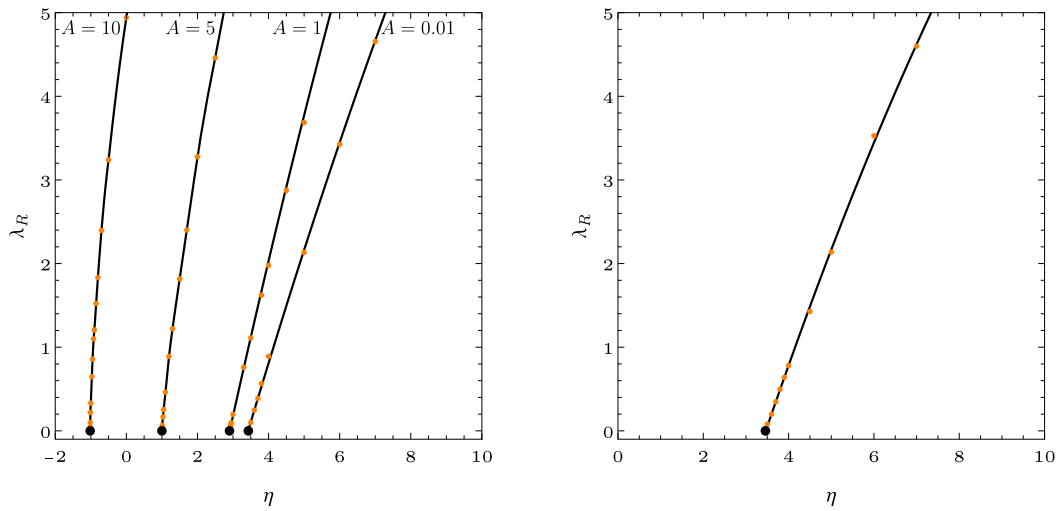


Fig. 8. Nonlinear stability results: the orange dots denote the growth rates while the black solid lines are plots of their interpolation. Left-hand frame: values of the growth rate λ_R for $n = 0$ plotted as function of η and for different values of the amplitude A . Right-hand frame: values of the growth rate λ_R for $n = 1, 2$ plotted as function of η for different values of A ; a single line is present since λ_R does not depend on A and n thus the data is superposed.

Table 2

The values of η that yield $\lambda_R = 0$ reported for different values of the amplitude A of the initial condition (21).

A	η		
	$n = 0$	$n = 1$	$n = 2$
10^{-4}	3.431	3.452	3.465
10^{-2}	3.431	3.448	3.445
10^{-1}	3.382	3.475	3.448
1	2.902	-	-
5	1.000	-	-
10	-1.018	-	-

also note that, for these nonlinear neutrally stable configurations, η is a monotonically decreasing function of the amplitude A : the threshold value of η for the onset of nonlinear instability decreases below its linear critical value. This suggests the presence of subcritical instabilities. Hence, compared with the linear stability analysis, a wider number of velocity profiles can experience the nonlinear onset of thermal convection. One may also note that, for sufficiently low values of the

perturbation amplitude A , the linear stability analysis results are recovered. The results obtained for $n = 1$ and $n = 2$ are not reported since they would be superposed to the dotted line.

5. Conclusions

The linear and nonlinear stability of a vertical fluid saturated porous circular pipe undergoing viscous dissipation is investigated. The pipe is impermeable and subject to a uniform and constant temperature at the boundaries. The viscous heating is the only effect triggering the thermal instability. A vertical pressure gradient is imposed and the basic stationary and fully developed state, displays dual solutions: for each value of the pressure gradient, two velocity profiles are obtained. Each basic solution is characterised by a different velocity profile and thus a different velocity at the pipe axis. Since the Gebhart number assumes, for everyday life applications, values that are much smaller than unity, the case of small Gebhart number is investigated. The linear stability analysis of the dual solutions is performed by employing the normal modes and by solving numerically the eigenvalue problem obtained. The nonlinear stability analysis of the dual solutions is investigated numerically.

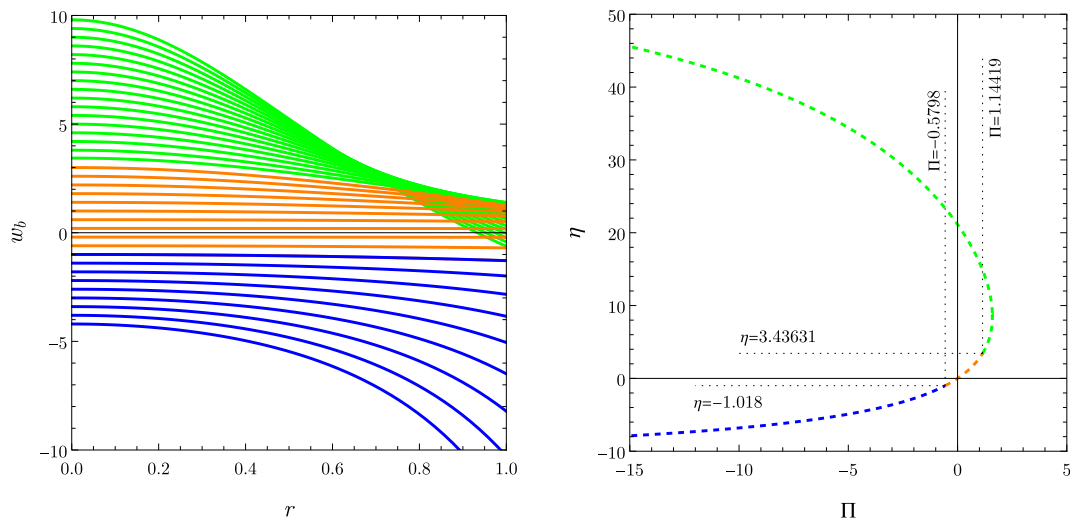


Fig. 9. Linear and nonlinear stability results obtained for $A = 10$ and $n = 0$: linearly unstable basic states, green color, nonlinearly unstable basic states, orange color, and stable basic states, blue color. (For interpretation of the references to color in this figure legend, the reader is referred to the web version of this article.)

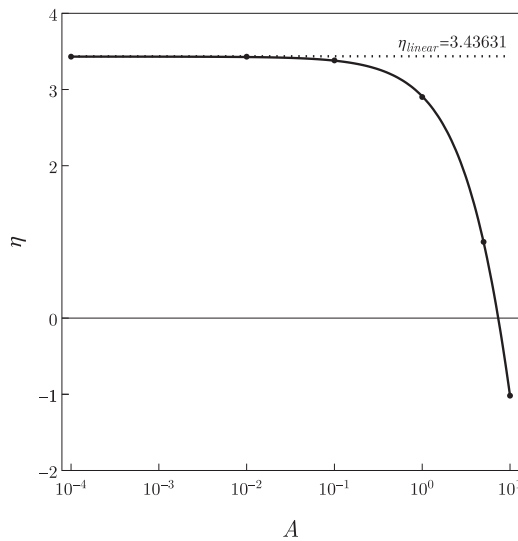


Fig. 10. Comparison between linear and nonlinear stability results: threshold values of η for the onset of nonlinear instability for $n = 0$, solid lines. The dotted line refers to the threshold value of η obtained by the linear stability analysis. The data obtained for $n = 1$ and $n = 2$ are not reported for the sake of readability since they would be superposed to the dotted curve.

ically by employing the finite element method. The main findings are the following:

- an innovative scaling is proposed to obtain the dimensionless formulation of the problem. This scaling allows to treat the case of small Gebhart numbers without neglecting the viscous dissipation contribution;
- basic stationary fully developed dual solutions are found. The vertical pressure gradient driving the basic flow displays a maximum value beyond which no stationary solutions exist;
- the axisymmetric modes are the only modes which can become linearly unstable;
- for the linear stability analysis, the most unstable modes are those with infinite wavelength and critical dimensionless velocity at the pipe axis equal to 3.43631;
- the nonlinear stability analysis retrieves the results obtained by the linear stability analysis when small values of the initial perturbation amplitude are considered;
- for sufficiently high values of the initial perturbation amplitude, the nonlinear stability analysis displays subcritical instabilities when the dimensionless amplitude is larger than 10^{-2} ;
- the most unstable initial perturbations are, for the nonlinear stability analysis, those characterised by the lowest spatial frequency. These

Appendix A. Cut-off parameter test

A test of the influence of the cut-off parameter ϵ on the solution is reported in Table A.3: the values of λ_R obtained by fixing the wavenumber, $k = 0$, the growth rate, $\eta = 6$ and $m = 0$ are displayed for different values of ϵ . From Table A.3, one can note that λ_R displays seven digits of precision already by considering $\epsilon = 10^{-5}$. The results presented throughout the paper are thus obtained by fixing $\epsilon = 10^{-10}$.

Table A.3
Values of η for different choices of ϵ by fixing $k = 0$, $\lambda_R = 0$ and $m = 0$.

ϵ	λ_R
10^{-1}	3.359134
10^{-2}	3.298679
10^{-3}	3.293563

(continued on next page)

perturbations display an initial exponential growth in time followed by a faster growth;

- the nonlinear evolution in time of the unstable perturbations characterised by a spatial frequency higher than for the most unstable modes displays a nonlinear saturation: for sufficiently long times an asymptotic equilibrium state is reached.

The linear stability analysis allows one to conclude that the critical wavenumber for the onset of instability is zero and the critical dimensionless velocity at the pipe axis is equal to 3.43631. The results of the nonlinear analysis display subcritical instabilities: the onset of instability is obtained for values of the governing parameters which are lower than the critical values obtained by the linear analysis. This feature occurs when the amplitude of the initial disturbance applied to the nonlinear problem is sufficiently high, namely when the dimensionless amplitude is larger than 10^{-2} .

CRedit authorship contribution statement

Michele Celli: Writing – review & editing, Writing – original draft, Visualization, Validation, Supervision, Software, Resources, Project administration, Methodology, Investigation, Funding acquisition, Formal analysis, Data curation, Conceptualization. **Antonio Barletta:** Writing – review & editing, Writing – original draft, Visualization, Validation, Supervision, Software, Resources, Project administration, Methodology, Investigation, Funding acquisition, Formal analysis, Data curation, Conceptualization. **Pedro Vayssi re Brand o:** Writing – review & editing, Writing – original draft, Visualization, Validation, Supervision, Software, Resources, Project administration, Methodology, Investigation, Funding acquisition, Formal analysis, Data curation, Conceptualization. **Silvia da Costa Hirata:** Writing – review & editing, Writing – original draft, Visualization, Validation, Supervision, Software, Resources, Project administration, Methodology, Investigation, Funding acquisition, Formal analysis, Data curation, Conceptualization. **Mohamed Najib Ouarzazi:** Writing – review & editing, Writing – original draft, Visualization, Validation, Supervision, Software, Resources, Project administration, Methodology, Investigation, Funding acquisition, Formal analysis, Data curation, Conceptualization.

Declaration of competing interest

The authors declare that they have no known competing financial interests or personal relationships that could have appeared to influence the work reported in this paper.

Data availability

No data was used for the research described in the article.

Table A.3 (continued)

ϵ	λ_R
10^{-4}	3.293464
10^{-5}	3.293462
10^{-6}	3.293462
10^{-7}	3.293462
10^{-8}	3.293462
10^{-9}	3.293462
10^{-10}	3.293462

Appendix B. Mesh test

In Table B.4 we analyse how the nonlinear simulations depend on the mesh employed. The mesh elements are triangular and the mesh is unstructured. For this mesh-test, the configuration $\eta = 5$, $A = 5$ and $n = 0$ has been chosen. The maximum measure (MaxCellMeasure) of the mesh elements has been reduced progressively from 10^{-1} to 10^{-4} . The values of the growth rates λ_R obtained for different mesh refinements, *i.e.* different values of MaxCellMeasure, are presented in Table B.4. From MaxCellMeasure equal to 10^{-3} , the values of λ_R display four digits of precision. The value of MaxCellMeasure employed for the nonlinear simulation is 10^{-3} .

Table B.4

Values of λ_R for different maximum measure of the mesh elements (“MaxCellMeasure”). The growth rate values are obtained for the case $\eta = 5$, $A = 5$ and $n = 0$.

MaxCellMeasure	λ_R
10^{-1}	9.562
10^{-2}	9.595
10^{-3}	9.593
10^{-4}	9.593

References

- [1] P.V. Brandão, L.S. de B. Alves, D. Rodríguez, A. Barletta, Linear disturbance growth induced by viscous dissipation in Darcy–Bénard convection with throughflow, *J. Fluid Mech.* 974 (2023) A15.
- [2] N. Deepika, P.A.L. Narayana, A.A. Hill, The nonlinear stability analysis of double-diffusive convection with viscous dissipation effect, *Transp. Porous Media* (2023) 1–13.
- [3] D. Yadav, M. Maqhusi, Influence of temperature dependent viscosity and internal heating on the onset of convection in porous enclosures saturated with viscoelastic fluid, *Asia Pac. J. Chem. Eng.* 15 (6) (2020) e2514.
- [4] D. Yadav, S.B. Nair, M.K. Awasthi, R. Ragoju, K. Bhattacharyya, Linear and nonlinear investigations of the impact of chemical reaction on the thermohaline convection in a permeable layer saturated with Casson fluid, *Phys. Fluids* 36 (1) (2024).
- [5] A. Barletta, Laminar mixed convection with viscous dissipation in a vertical channel, *Int. J. Heat Mass Transf.* 41 (22) (1998) 3501–3513.
- [6] A. Barletta, Combined forced and free convection with viscous dissipation in a vertical circular duct, *Int. J. Heat Mass Transf.* 42 (12) (1999) 2243–2253.
- [7] A. Barletta, E. Magyari, B. Keller, Dual mixed convection flows in a vertical channel, *Int. J. Heat Mass Transf.* 48 (23–24) (2005) 4835–4845.
- [8] A. Barletta, S. Lazzari, E. Magyari, Buoyant Poiseuille–Couette flow with viscous dissipation in a vertical channel, *Z. Angew. Math. Phys.* 59 (2008) 1039–1056.
- [9] A. Barletta, M. Celli, Mixed convection MHD flow in a vertical channel: effects of Joule heating and viscous dissipation, *Int. J. Heat Mass Transf.* 51 (25–26) (2008) 6110–6117.
- [10] A.E. Gill, A. Davey, Instabilities of a buoyancy-driven system, *J. Fluid Mech.* 35 (4) (1969) 775–798.
- [11] C.M. Vest, V.S. Arpaci, Stability of natural convection in a vertical slot, *J. Fluid Mech.* 36 (1) (1969) 1–15.
- [12] S.A. Korpela, D. Gözüüm, C.B. Baxi, On the stability of the conduction regime of natural convection in a vertical slot, *Int. J. Heat Mass Transf.* 16 (9) (1973) 1683–1690.
- [13] G.D. McBain, S.W. Armfield, Natural convection in a vertical slot: accurate solution of the linear stability equations, *ANZIAM J.* 45 (2003) C92–C105.
- [14] B. Straughan, Nonlinear stability for thermal convection in a Brinkman porous material with viscous dissipation, *Transp. Porous Media* 134 (2) (2020) 303–314.
- [15] D.A.S. Rees, E. Magyari, Hexagonal cell formation in Darcy–Bénard convection with viscous dissipation and form drag, *Fluids* 2 (2) (2017) 27.
- [16] A. Barletta, G. Mulone, The energy method analysis of the Darcy–Bénard problem with viscous dissipation, *Contin. Mech. Thermodyn.* 33 (2021) 25–33.
- [17] M. Miklavcic, C.Y. Wang, Completely passive natural convection, *Z. Angew. Math. Mech.* 91 (2011) 601–606.
- [18] M. Miklavcic, Stability analysis of some fully developed mixed convection flows in a vertical channel, *Z. Angew. Math. Mech.* 95 (9) (2015) 982–986.
- [19] D.A. Nield, A. Bejan, *Convection in Porous Media*, 5th edition, Springer, New York, 2017.
- [20] A. Barletta, M. Celli, D.A.S. Rees, The onset of convection in a porous layer induced by viscous dissipation: a linear stability analysis, *Int. J. Heat Mass Transf.* 52 (1–2) (2009) 337–344.
- [21] A. Barletta, M. Miklavcic, On fully developed mixed convection with viscous dissipation in a vertical channel and its stability, *Z. Angew. Math. Mech.* 96 (12) (2016) 1457–1466.